Supporting Information for the manuscript of

"Heteroatom-Doped Reduced Graphene Oxide Electrochemical Sensor for Sensitive Dopamine Detection with Preliminary Clinical Evaluation of Neurotransmitter Dysregulation in Pediatric Epilepsy"

SI.1. Results

SI.1.1 Structural and Morphological Characterization

The surface morphology of the synthesized X-RGO materials (X= N, (S/N)) was examined using scanning electron microscopy (SEM) (**Fig. S1A**). The SEM image of GO (**Fig. S1A-a**) displayed a typical layered structure with a smooth surface, attributed to well-separated graphene sheets and oxygenated functional groups **[1-3]**. In contrast, N-RGO and (S/N)-RGO (**Fig. S1A-b and 1A-c**), obtained through solvothermal reduction and heteroatom doping, exhibited pronounced wrinkling and exfoliation, indicative of increased surface roughness and structural distortion. Compared to (S/N)-RGO, N-RGO exhibited more pronounced wrinkling and stacked layered features, suggesting that nitrogen incorporation induced substantial lattice reconfiguration and partial restacking of graphene sheets. These morphological modifications, characterized by increased surface defects and disoriented graphene sheets, arise from the synergistic effects of thermal annealing and heteroatom doping **[4-6]**, which are known to improve electrochemical activity. Energy-dispersive X-ray (EDX) spectroscopy (**Fig. S1B**) confirmed the successful incorporation of nitrogen and sulfur within the N-RGO and (S/N)-RGO, respectively. Elemental analysis (**Table S1**) revealed doping levels of 2% regarding carbon for N-RGO and 20% for (S/N)-RGO. In (S/N)-RGO, sulfur and nitrogen were distributed at 13.7% and 6.3%, respectively, demonstrating effective co-doping and suggests potential synergistic interactions between the two heteroatoms, which can modulate electronic density and enhance active site distribution, thereby promoting electrochemical performance **[7]**. X-ray diffraction (XRD) analysis (**Fig. S1C**) showed that both N-RGO and (S/N)-RGO displayed broad peaks at $2\theta = 25.31°$ and 24.27°, associated with the (002) plane of graphitic carbon. Compared to the sharp peak of GO (**Fig. S1C-a**), the broader peaks observed in the doped samples indicate increased structural disorder and partial reduction **[8]**. The interlayer spacings, calculated to be 0.35 nm for N-RGO and 0.37 nm for (S/N)-RGO, were significantly smaller than that of GO (0.81 nm) **[9,10]**, confirming effective reduction and reconstitution of the conjugated carbon network. Fourier-transform infrared (FT-IR) spectroscopy (**Fig. S1D**) provided complementary insights. The disappearance of the C=O stretching vibration at 1735 cm^{-1} in X-RGO confirmed successful reduction of GO **[11]**. Moreover, the shift of the C=C stretching band from 1596 cm^{-1} (GO) to 1625 cm^{-1} (X-RGO) indicated the partial restoration of the sp^2-hybridized carbon network **[1]**. The broad absorption around 3420 cm^{-1} corresponded to O-H, N-H, or S-H vibrations, suggesting the presence of residual hydroxyl, amine, or thiol groups **[12]**. A distinct C-N stretching

band at 1120 cm^{-1} in N-RGO validated nitrogen incorporation **[13]**, while the additional peaks at 1047 cm^{-1} and 1402 cm^{-1} in (S/N)-RGO were attributed to C-N and C-S stretching vibrations, confirming successful co-doping of nitrogen and sulfur **[14-16]**. Raman spectroscopy (**Fig. S1E**) further supported the structural transformation. All samples exhibited the characteristic D and G bands, corresponding to the disordered and graphitic sp^2 carbon atoms, respectively **[18]**. The intensity ratio ($\frac{ID}{IG}$) increased significantly upon doping, from 0.52 for GO to 1.81 for N-RGO and 1.35 for (S/N)-RGO (**Fig. S2B, Table S2**). This pronounced enhancement reflects the introduction of structural defects and heteroatoms into the graphene framework, which facilitate charge transfer and enhance electrochemical activity **[17]**.

Overall, these results confirm that heteroatom doping effectively modified the morphology, composition, and structure of RGO, generating a more electroactive surface with abundant defect sites, key factors responsible for the superior electrochemical performance for the nanomaterials.

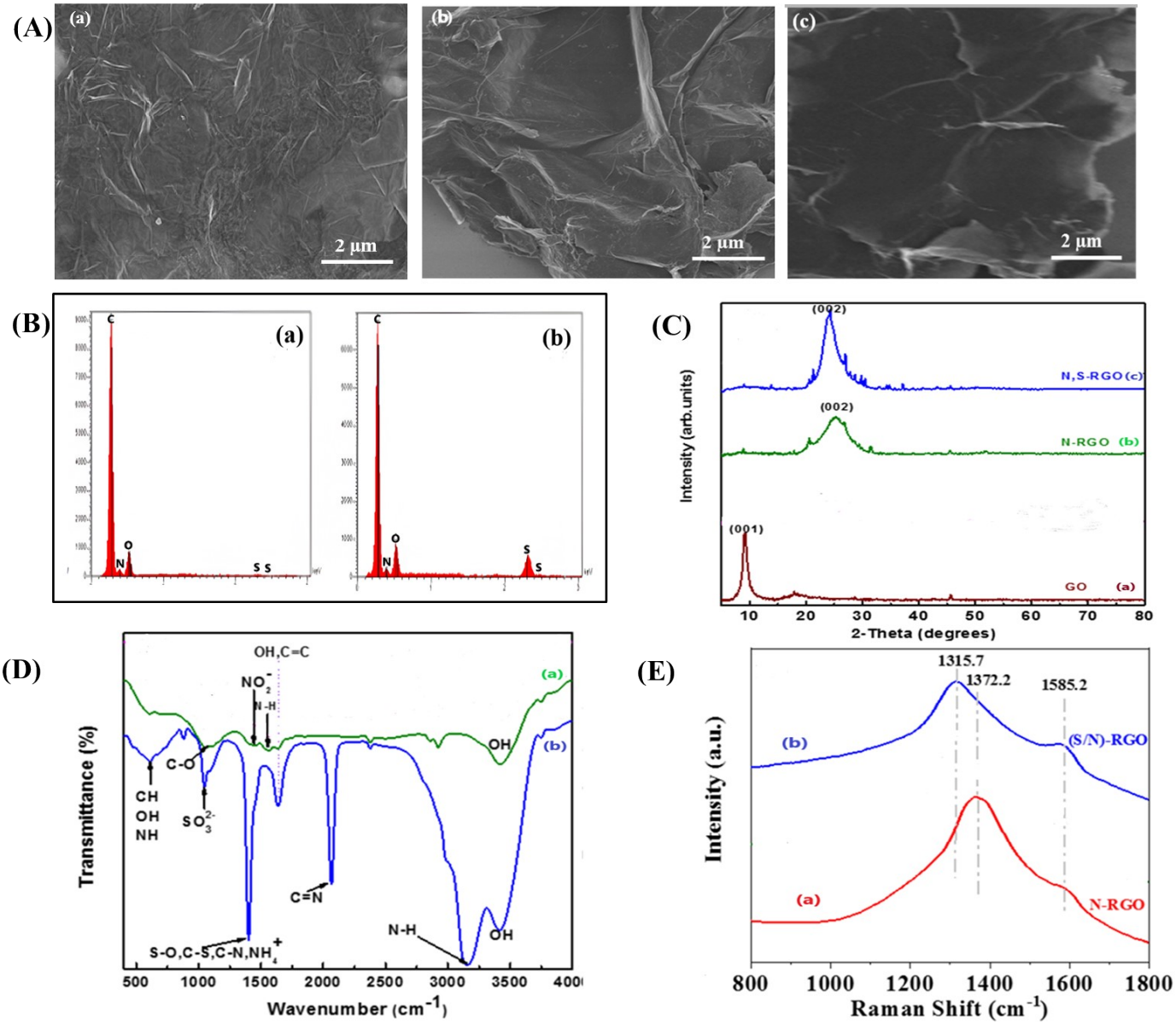

Fig. S1 Structural and morphological characterization of the synthesized materials. **(A)** SEM images of **(a)** GO, **(b)** N-RGO, and **(c)** (S/N)-RGO. **(B)** EDX elemental mapping of **(a)** N-RGO and **(b)** (S/N)-RGO confirming the

presence of nitrogen and sulfur dopants. **(C)** XRD patterns of **(a)** GO, **(b)** N-RGO, and **(c)** (S/N)-RGO showing variations in crystallinity and interlayer spacing. **(D)** FT-IR spectra of **(a)** N-RGO and **(b)** (S/N)-RGO highlighting functional group transformations upon reduction and doping. **(E)** Raman spectra of **(a)** N-RGO and **(b)** (S/N)-RGO showing D and G bands, with ID/IG ratios indicating defect levels.

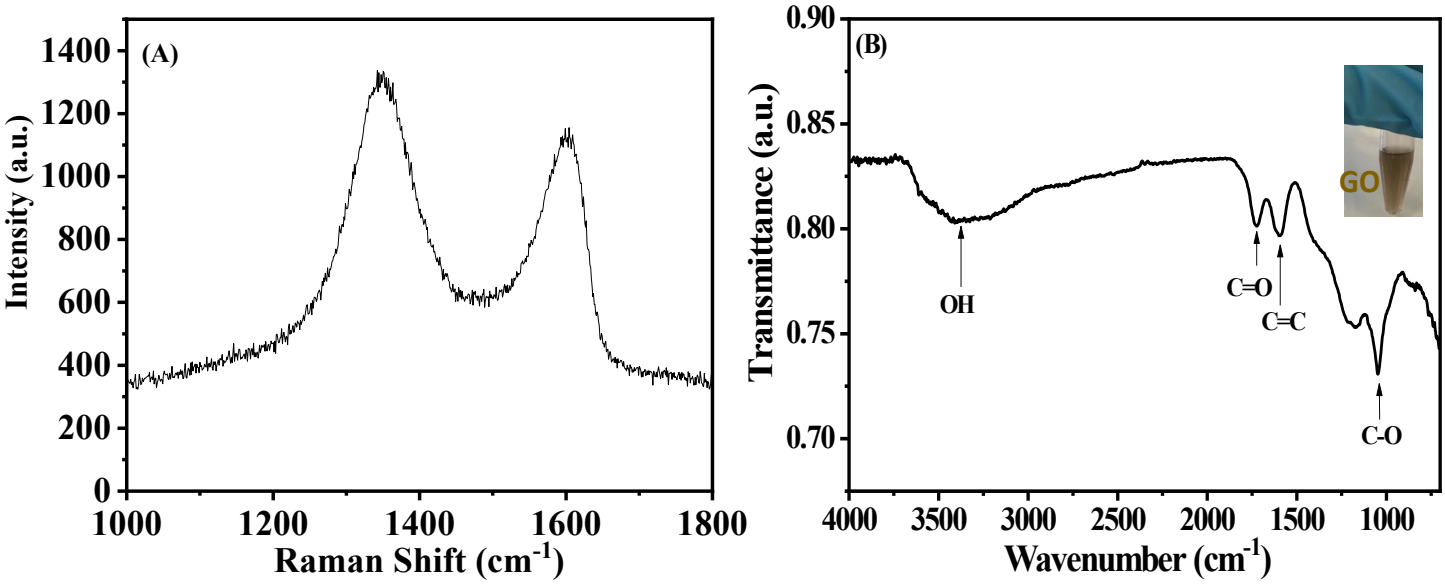

Fig. S2 (A) Raman spectra and **(B)** FT-IR spectra of GO.

Table S1 EDX analysis results of X-RGO samples

Elements atomic %	Carbon C	Oxygen O	Sulfur S	Nitrogen N
N-RGO	86.67	10.00	0.00	3.33
(S/N) -RGO	72.74	13.63	9.09	4.54

Table S2 Peak Positions of D and G Raman bands and I_D/I_G for GO, N-RGO and (S/N)-RGO are presented in this table

Sample	D band	G band	ID/IG
GO	1355	1580	0.52
N-RGO	1372	1585	1.81
(S/N)-RGO	1315	1585	1.35

SI.1.2 Electrochemical characterization

Table S3 Results of electrochemical measurements on the modified electrodes in $[Fe(CN)_6]^{-3/-4}$solutionis presented in this table

Modified GCE	Anodic intensity I_{pa}(µA)	Cathodic intensity I_{pc} (µA)	Oxidation potential $E_{pa}(V)$	Reduction potential $E_{pc}(V)$	Potential Difference ΔE_p (V)
RGO/GCE	27.821	-26.971	0.254	0.135	0.119
N-RGO/GCE	39.305	-37.233	0.250	0.163	0.087
(S/N)-RGO/GCE	122.109	-118.552	0.249	0.152	0.097

Table S4 Results of electrochemical measurements on the modified electrodes in $[Ru(NH_3)]_6^{3+/2+}$ solution is presented in this table.

Modified GCE	Anodic intensity I_{pa}(µA)	Cathodic intensity I_{pc} (µA)	Oxidation potential $E_{pa}(V)$	Reduction potential $E_{pc}(V)$	Potential Difference ΔE_p (V)
RGO/GCE	3.199	-9.382	-0.165	-0.246	0.042
N-RGO/GCE	4.451	-11.687	-0.167	-0.234	0.040
(S/N)-RGO/GCE	9.871	-48.226	-0.168	-0.265	0.043

Table S5 Impedance data obtained for the modified electrodes in $[Fe(CN)_6]^{3-/4-}$ (10 mM, 0.1 M KCL). All values were obtained from the fitted impedance spectra.

	RGO/GCE		N-RGO/GCE		(S/N) -RGO/GCE	
	Result	**Error (%)**	**Result**	**Error (%)**	**Result**	**Error (%)**
Rs(Ω)	604.31	0.42	608.34	0.725	615.16	0.389
RCT(Ω)	1502.9	0.5	996.79	1.177	1111.8	0.620
CPE (µF)	1.982	3.744	4.566	7.877	3.301	4.169
n	0.925	0.592	0.834	1.390	0.889	0.697
W (µF)	0.0023	3.269	0.0022	3.937	0.0023	2.573

Table S6 Impedance data obtained for the modified electrodes in $[Ru(NH_3)_6]^{2+/3+}$ (10 mM, 1M KCL). All values were obtained from the fitted impedance spectra.

	RGO/GCE		N-RGO/GCE		(S/N) -RGO/GCE	
	Result	Error (%)	Result	Error (%)	Result	Error (%)
Rs (Ω)	2713.3	0.905	1080.7	0.102	5495.7	0.100
R_{CT} (Ω)	-	-	40853	16.823	63995	9.379
CPE (µF)	20.846	1.603	3.103	1.821	3.282	5.251
n	0.839	0.829	0.924	0.292	0.945	0.902
CPE1 (µF)	-	-	1.508	3.308	1.479	5.741
n 1	-	-	0.608	0.791	0.555	2.181

SI.1.3 Effect of Scan Rate and Kinetic Analysis

SI.1.3.1 Electroactive Surface Area of the Modified Electrodes

The electrochemical behavior and effective surface area of the modified electrodes (RGO/GCE, N-RGO/GCE, and (S/N)-RGO/GCE), were investigated using both outer-sphere $[Fe(CN)_6]^{3-/4-}$ and inner-sphere $[Ru(NH_3)_6]^{2+/3+}$ redox probes. The electroactive surface areas were calculated from Randles-Sevcik equation (**Eq.1**):

$$I_p = 2.69 \times 10^5 \times n^{\frac{3}{2}} A_{area} \times D^{\frac{1}{2}} \times v^{\frac{1}{2}} \times C \qquad \textbf{Eq. 1}$$

where I_p is the oxidation peak current (A), n is the number of electrons transferred, A_{area} is the electroactive surface area (cm^2), D is the diffusion coefficient ($cm^2\ s^{-1}$), C is the concentration of the redox probe (mol cm^{-3}) and v is the scan rate (Vs^{-1}).

As shown in **Fig. S3**, cyclic voltammograms were recorded in 10 mM $[Fe(CN)_6]^{3-/4-}$ solution, at scan rates ranging from 50 to 500 mVs^{-1}.

For estimating the electrochemical surface areas, we used the slope of the linear dependence of I_p on $v^{\frac{1}{2}}$ given by (**Eq.1**) for an inner- and outer -sphere redox probes. Results listed in **Table 1** show the significant enhancement of A_{area} for the doped materials, due to nitrogen, sulfur/ nitrogen co-doping that improve the number of active sites and improve electronic conductivity. Similar results were observed when $[Ru(NH_3)_6]^{2+/3+}$ was used as an inner-sphere probe (**Fig. S4**), indicating that the improvement is not probe-dependent but intrinsic to the doped RGO structure.

SI.2.3.2 Assessment of Electron Transfer Kinetics at the Modified Electrodes

Heterogeneous Electron Transfer Rate Constant (k_0)

The heterogeneous electron transfer rate constant (k_0) was determined using the method of Nicholson combined with the Lavagnini et al method, which is suitable to quasi-reversible systems **[19]**. The relationship between the dimensionless parameter (ψ) and k_0 is given by (**Eq. 2):**

$$\psi = k_0[(\pi D n v F)/(RT)]^{\frac{1}{2}} \qquad \textbf{Eq. 2}$$

Where D is the diffusion coefficient of the redox species, n is the number of transferred electrons, F is the Faraday constant, R is the molar gas constant, T is the absolute temperature and v is the scan rate. For quasi-reversible systems, ψ can be estimated from (**Eq.3**):

$$\psi = (-0.6288 + 0.0021X)/(1 - 0.017X) \qquad \textbf{Eq. 3}$$

Where $X = \Delta E_p$ (mV), $and\ \Delta E_p$= Epa-Epc represents the peak-to-peak separation between the anodic and cathodic peaks. Through this mathematical manipulation, k_0 is obtained from the slope of the graph of ψ versus $v^{-1/2}$.

Determination of the Diffusion Constant (D_0)

The diffusion coefficient (D_0), required for the above analyses can be determined from the quasi-reversible Randles-Sevcík equation, which relates the peak current, Ip, to the scan rate,υ **[20][21]**.

$$I_{p,quasi} = (2.65\times10^5)\ n^{3/2}\ A\ D_0^{1/2}\ C\ \upsilon^{1/2} \qquad \textbf{Eq. 4}$$

where D_0 is the diffusion coefficient of the electroactive probe, A is the geometric electrode area (cm^2), n is the number of electrons transferred in the electrochemical process, C is the concentration of the redox probe and υ is the applied voltammetric scan rate ($V\ s^{-1}$).

For all the redox markers and the modified surfaces, Relationship of ΔEp and ψ versus $v^{-\frac{1}{2}}$ are displayed in (**Figures. S5-S6**). These results confirm that the doped RGO electrodes possess faster electron transfer kinetics, attributed to the enhanced conductivity and defect-induced active sites introduced by heteroatom doping.

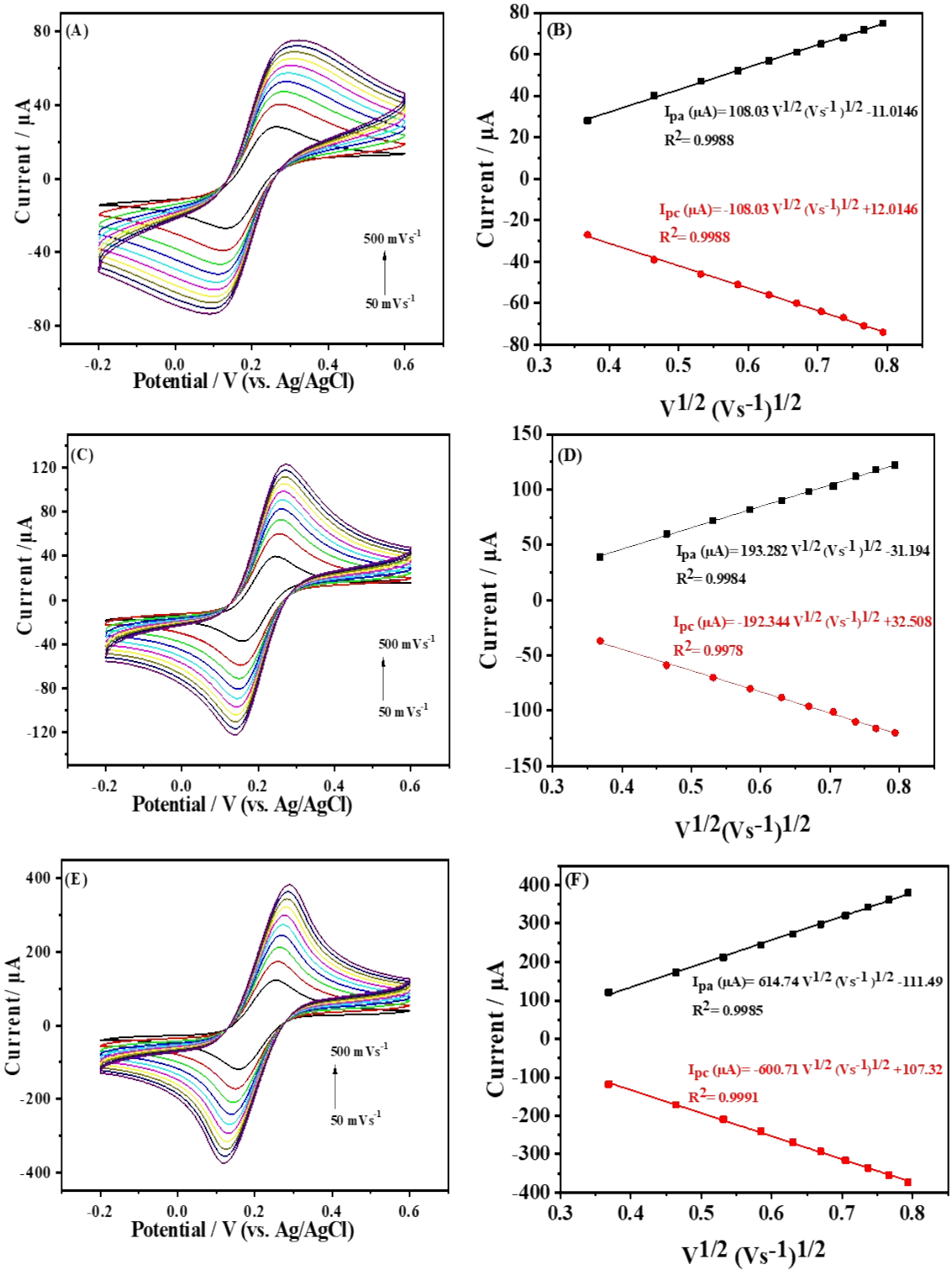

Fig. S3 (A, C, E) CV curves of RGO, (S/N)-RGO and N-RGO/GCEs at different scan rates in 10 mM $[Fe(CN)_6]^{3-/4-}$ solution. **(B, D and F)** The linear relationship between the anodic and cathodic peak currents versus scan rate.

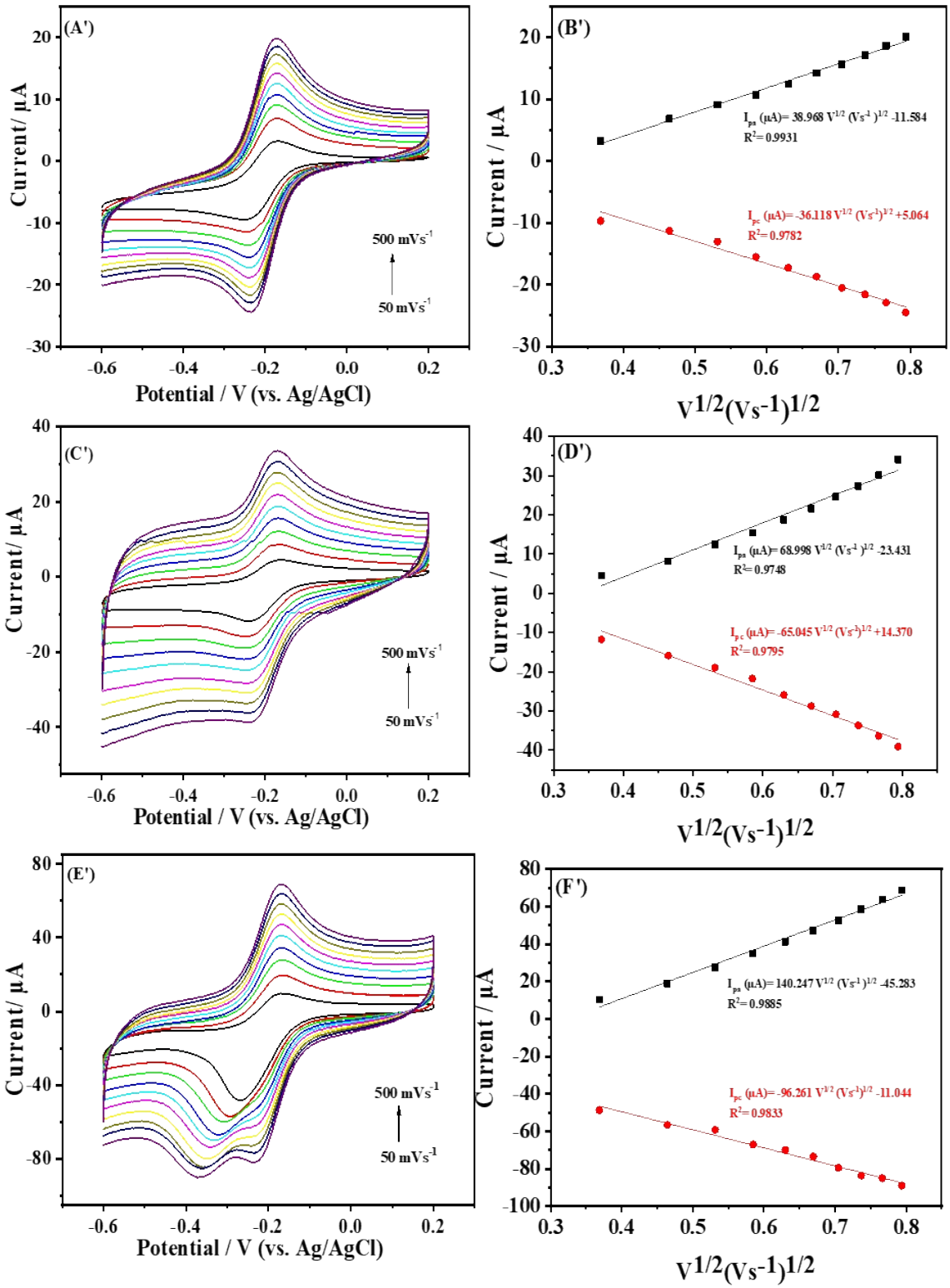

Fig. S4 (A', C' and E') CV curves of RGO, N-RGO and (S/N)-RGO/GCEs at different scan rates in 10 mM $[Ru(NH_3)_6]^{2+/3+}$ solution. **(B', D'and F')** The linear relationship between the anodic and cathodic peak currents versus scan rate**.**

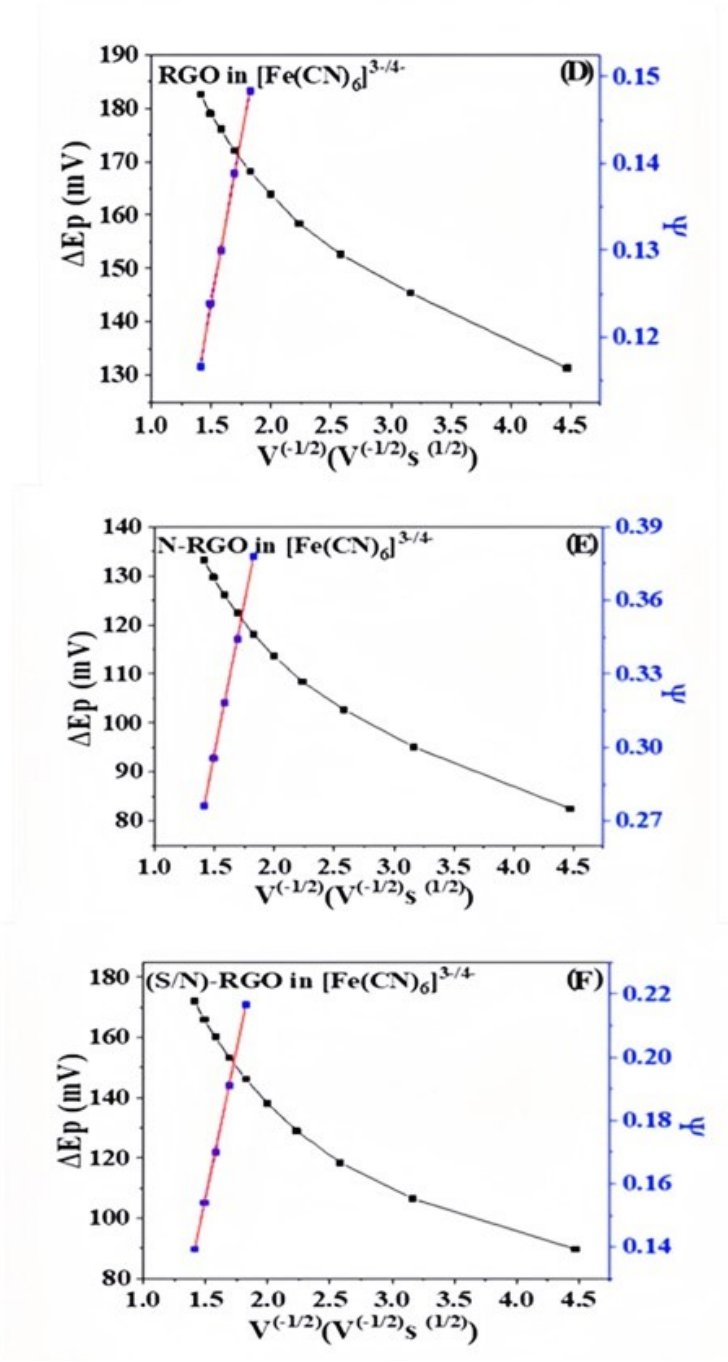

Fig. S5. Relationship of ΔE_p and ψ versus $V^{-1/2}$ of **(D)** RGO, **(E)** N-RGO and **(F)** (S/N)-RGO using $[Fe(CN)_6]^{3-/4}$ redox marker.

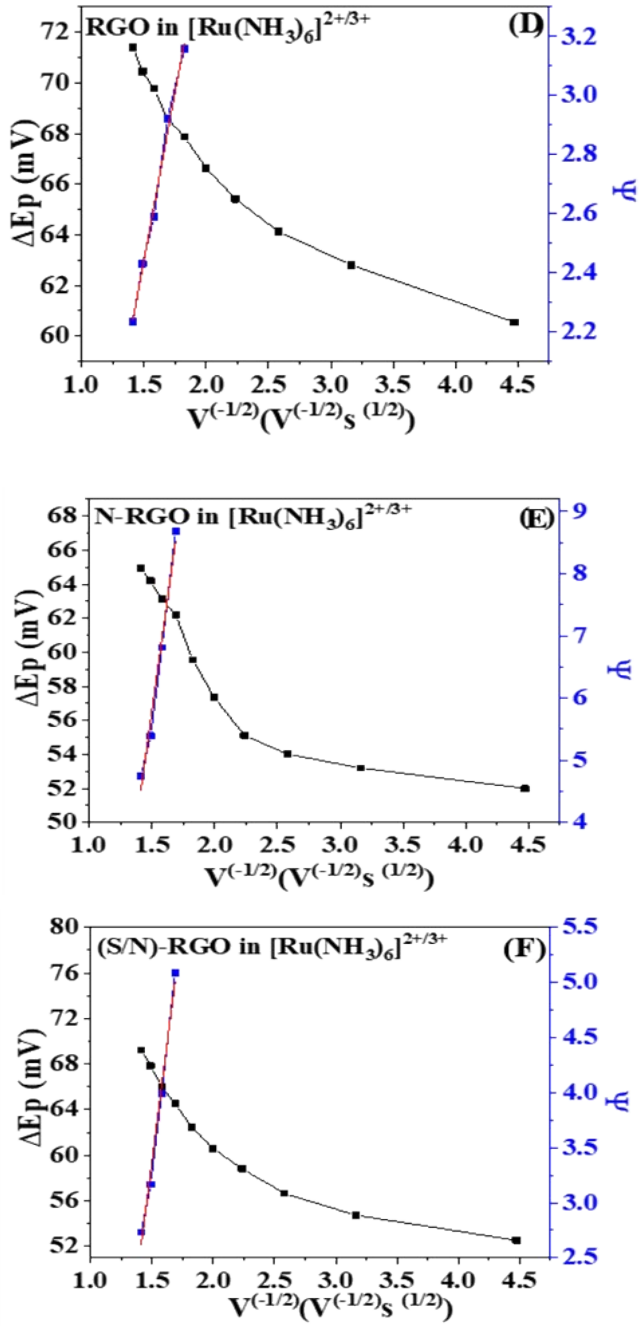

Fig. S6. Relationship of ΔE_p and ψ versus $V^{-1/2}$ of **(D)** RGO, **(E)** N-RGO and **(F)** (S/N)-RGO using $[Ru(NH_3)_6]^{2+/3+}$ redox marker.

SI.1.4. Determination of Dopamine in Real Samples

The % recovery values of the spiked DA samples calculated using equations 5 and 6 indicating insignificant impact of test-sample matrix on the sensor response.

$$\% \text{ Recovery (Commercial plasma sample)} = \frac{Concentration\ Founded}{Concentration\ Added} * 100 \quad \textbf{Eq.5}$$

$$\% \text{ Recovery (Human serum sample)} = \frac{Concentration\ Founded}{(Concentration\ Added + C0)} * 100 \quad \textbf{Eq.6}$$

Here, Co is the experimentally obtained concentrations of DA in unspiked serum samples. Thus, detailed characterization and response studies show that our sensor is highly suitable for reliable and sensitive detection of DA in biological samples

SI.1.5 Electrochemical DA Sensor in the Clinical Field

Fig. S7 presents the DPV responses for the detection of DA in commercial plasma samples. Successive standard additions of DA were performed, and a clear increase in peak current was observed with each addition. The resulting linear regression equation is: I(μA) =0.440+5.375x (μM) with an excellent correlation coefficient of R^2=0.975, confirming the good linearity and sensitivity of the method in this range.

This calibration plot was used to determine the unknown initial DA concentration in blood samples collected from epileptic children.

To determine the DA concentration, the corresponding oxidation current (**Fig. S8**) was projected onto the calibration curve (**Fig. S7B**). By intersecting the current value with the linear calibration line, the corresponding DA concentration was directly read from the x-axis. This approach allowed us to estimate the initial DA levels in clinical samples (e.g., serum from epileptic children) without the need for DA addition, confirming the applicability of the method for real sample analysis.

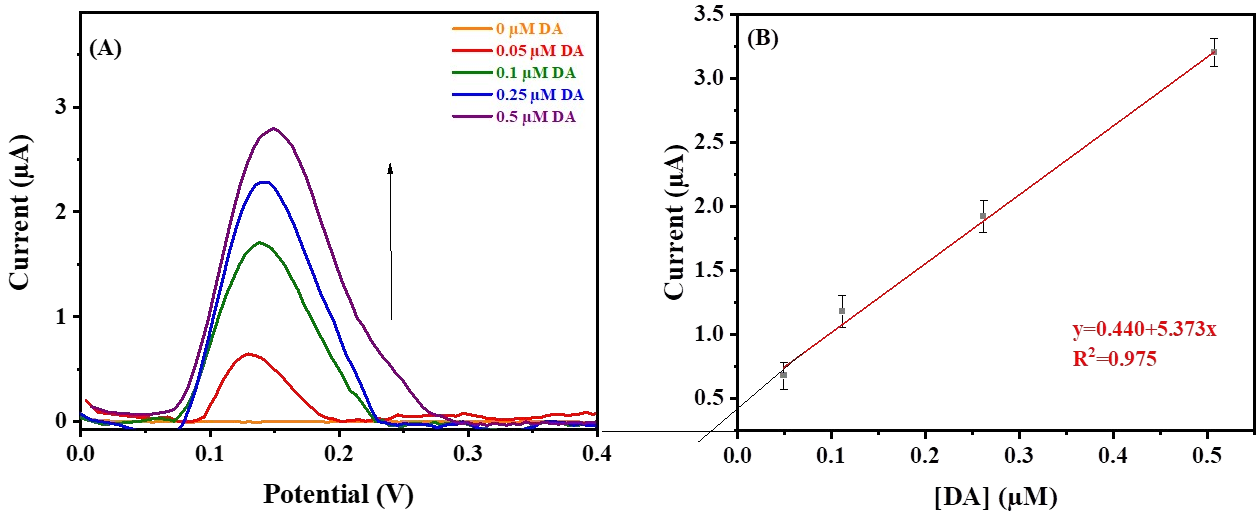

Fig. S7 DPV recorded at a scan rate of 50 mVs^{-1} from the measurement of 0.1 M phosphate buffer (pH 7.0) solution containing: **(A)** commercial plasma sample (without addition of DA) spiked with various concentrations of DA using SPCE/N-RGO. **(B)** Calibration plot of the concentration of DA.

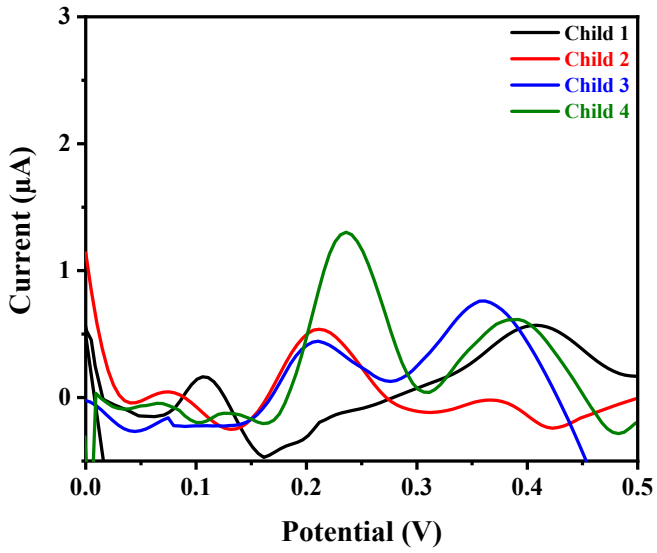

Fig. S8 DPV recorded at a scan rate of 50 $mV \cdot s^{-1}$ for the measurement of a solution containing blood serum samples from children's patients with epilepsy.

References

1. Z. Hsine, S. Bizid, R. Mlika, et al., *Sensors*, 2020, 20, 1256, DOI: 10.3390/s20051256.
2. Z. Su, H. Wang, K. Tian, et al., *Compos. Part A Appl. Sci. Manuf.*, 2016, 84, 64-73, DOI: 10.1016/j.compositesa.2015.11.033.
3. M. Sabbaghan, H. Charkhan, M. Ghalkhani and J. Beheshtian, *Res. Chem. Intermed.*, 2019, 45, 487-505, DOI: 10.1007/s11164-018-3613-8.
4. F. Razmjooei, K. P. Singh, M. Y. Song and J. S. Yu, *Carbon*, 2014, 78, 257-267, DOI: 10.1016/j.carbon.2014.07.002.
5. X. Duan, K. O'Donnell, H. Sun, et al., *Small*, 2015, 11, 3036-3044, DOI: 10.1002/smll.201403715.
6. Z. Tian, J. Li, G. Zhu, et al., *Phys. Chem. Chem. Phys.*, 2016, 18, 1125-1130, DOI: 10.1039/C5CP05475C.

7. D. Li, C. Yu, M. Wang, et al., *RSC Adv.*, 2014, 4, 55394-55399, DOI: 10.1039/C4RA10761F.
8. P. Sun, H. Liu, M. Feng, et al., *Appl. Catal. B Environ.*, 2019, 242, 335-345, DOI: 10.1016/j.apcatb.2019.03.085.
9. H. Cheng, X. Zhou, A. Gao, et al., *Electrochim. Acta*, 2018, 292, 2030, DOI: 10.1016/j.electacta.2018.09.092.
10. M. Domga, F. Karnan, G. B. Oladoyinbo, et al., *Electrochim. Acta*, 2020, 341, 135999, DOI: 10.1016/j.electacta.2020.135999.
11. L. Zhang, X. Qing, Z. Chen, et al., *ACS Appl. Energy Mater.*, 2020, 3, 6845-6852, DOI: 10.1021/acsaem.0c00952.
12. B. Amanulla, K. N. Perumal and S. K. Ramaraj, *Sens. Actuators B Chem.*, 2019, 281, 281-287, DOI: 10.1016/j.snb.2018.10.039.
13. S. Gu, C. T. Hsieh, Y. Y. Tsai, et al., *ACS Appl. Nano Mater.*, 2019, 2, 790-798, DOI: 10.1021/acsanm.8b02010.
14. Z. S. Schroer, Y. Wu, Y. Xing, et al., *ACS Appl. Nano Mater.*, 2019, 2, 6858-6865, DOI: 10.1021/acsanm.9b01309.
15. R. A. Rochman, S. Wahyuningsih, A. H. Ramelan and Q. A. Hanif, *IOP Conf. Ser. Mater. Sci. Eng.*, 2019, 509, 012119, DOI: 10.1088/1757-899X/509/1/012119.
16. J. Liu, X. Wang, Q. Lu, et al., *J. Electrochem. Soc.*, 2016, 163, A2360-A2367, DOI: 10.1149/2.0831614jes.
17. D. H. Youn, S. K. Stauffer, P. Xiao, et al., *ACS Nano*, 2016, 10, 10778-10788, DOI: 10.1021/acsnano.6b04214.
18. A. Shanmugasundaram, V. Gundimeda, T. Hou and D. W. Lee, *ACS Appl. Mater. Interfaces*, 2017, 9, 31728-31740, DOI: 10.1021/acsami.7b06253.
19. I. Lavagnini, R. Antiochia and F. Magno, *Electroanalysis*, 2004, 16, 505-506, DOI: 10.1002/elan.200302851.
20. D. A. C. Brownson, G. C. Smith and C. E. Banks, *R. Soc. Open Sci.*, 2017, 4, 171128, DOI: 10.1098/rsos.171128.
21. A. G. M. Ferrari, H. M. Elbardisy, V. Silva, T. S. Belal, W. Talaat, H. G. Daabees, C. E. Banks and D. A. C. Brownson, *Anal. Methods*, 2020, 12, 2133-2142, DOI: 10.1039/D0AY00169D.

Ethical Approval